Testing RM Inversion Methods

S. W. Mangham,[1]* K. Horne,[2] A. Pancoast, [3] P. Williams, [3] C. Knigge,[1] J. H. Matthews
and N. Higginbottom[1]

[1] *Department of Physics and Astronomy, University of Southampton, Southampton, SO17 1BJ, UK*
[2] *School of Physics and Astronomy, University of St. Andrews, North Haugh, St. Andrews KY16 9SS, UK*
[3] *Harvard-Smithsonian Center for Astrophysics, Garden Street, Cambridge, MA 02138, USA*
[4] *University of Oxford, Astrophysics, Keble Road, Oxford, OX1 3RH, UK*
[5] *Space Telescope Science Institute, 3700 San Martin Drive, Baltimore, MD 21218, USA*
[6] *Eureka Scientific, Inc., 2452 Delmer St., Suite 100, Oakland, CA 94602-3017, USA*
[7] *School of Mathematics and Physics, Queen's University Belfast, University Road, Belfast, BT7 1NN, UK*

ABSTRACT
Max 250 words.

- VR-RM is key in shaping understanding of AGN geometry
- Intent is to test accuracy of recovered RM
- Self-consistent RT & ion code capable of negative response
- FINDINGS: Positive results
- FINDINGS: Negative results
- General conclusions on limits of RM

Key words: accretion discs – radiative transfer – quasars: general

1 INTRODUCTION

Reverberation mapping (RM) is a highly useful tool for exploring the properties of Active Galactic Nuclei (AGN; Peterson (1993)). As the continuum of an AGN varies, the broad emission lines (BEL) in its spectra respond with a lag on the order of hours to months, depending on the luminosity of the system and the ionisation lines involved (Onken et al. 2004; Kaspi & Netzer 1999; Kaspi et al. 2005). By associating these lags with the light travel times of the system, it is possible to characterise the size of the broad emission line region (BLR) as $r = c\tau$. BELs have substantial Doppler broadening assumed to be from rotational motion, from which the Keplerian orbital velocity v_{BLR} at their characteristic radius r can be calculated, and from the two the super-massive black hole mass can be found as $M_{BH} \simeq c\tau_{BLR}v_{BLR}^2/G$.

Whilst a lag can be associated straightforwardly with a single characteristic radius, depending upon the geometry of the BLR and the incidence of the system to the observer emission at a single radius can be spread across a broad range of times. In theory, this allows a deconvolution of the light-curve of a BEL and the driving continuum to give a 1-dimensional response function. In practise, especially for geometries where emission is not generated at a single radius but across a distribution of radii, these 1-d response func-

tions are highly degenerate. For time series of spectra with sufficiently high velocity resolution it is possible to instead construct a 2-dimensional response function by deconvolving these spectra and the driving continuum light curve. These *velocity-resolved* response functions are specific to the geometry and kinematics of the BLR and offer a powerful tool with which to investigate behaviour at unresolvably small scales (Welsh & Horne 1991). Inflows and outflows in particular have very distinct signatures in a velocity-resolved response function (**???**).

Recent high-resolution observational campaigns (De Rosa et al. 2015; Du et al. 2014) have provided data from which these velocity-resolved response functions can be recovered (Grier et al. 2013; Pancoast et al. 2014). These efforts have produced a wide range of signatures, from simple rotation to both inflows (Ulrich & Horne 1996; Grier 2013; Bentz et al. 2008; Bentz et al. 2010; Gaskell 1988; Koratkar & Gaskell 1989) and outflows (Denney et al. 2009; Du et al. 2016). The variety of responses recovered suggests either that the BLR is a more varied region than geometric unification models propose, or that not all features of the response functions of real-world BLRs may be able to be recovered with current methods at current rates of observation.

In order to validate current deconvolution techniques, it is necessary to test them in a controlled manner against *known* response functions. By starting with the response function for a physically-motivated BLR, and using it to

* E-mail: s.w.mangham@soton.ac.uk

produce a time series of spectra comparable to those from observing campaigns like De Rosa et al. (2015) we can place limits on the type and level of detail we can expect current deconvolution techniques to recover a response function. In a previous paper (Mangham et al. 2017) we used a radiative transfer and ionisation code (Long & Knigge 2002) to produce physically-motivated response functions for one candidate BLR geometry, a rotating biconical disk wind (Shlosman & Vitello 1993). We take this response function and, using a real UV light curve (Fausnaugh et al. 2016), generate a fake observing campaign. The time series of spectra from this simulated observing campaign are then analysed using the MEMEcho (Horne et al. 1991; Horne 1994) and Caramel (Pancoast et al. 2011) deconvolution tools. We compare the recovered response functions for two types of template response functions; one that fits traditional assumptions about response function behaviour (i.e. linear positive response with increasing luminosity) and one that whilst equally physically plausible does *not* fit traditional assumptions.

The remainder of this paper is organised as follows. In section 2, we outline the theory behind RM and describe the assumptions and limits of inversion. In section 3, we describe the radiative transfer and ionisation code used to generate the response functions, and how our response functions are then used to generate the time series of spectra in the fake observing campaign. The authors of the inversion tools Caramel and MEMEcho then describe their respective methods. In section 4 for both methods we compare the recovered response functions to the response functions used to generate the time series of spectra, and in section 5 we discuss the implications of these comparisons. Finally, in section 6 we summarise the results of this work.

2   BACKGROUND

2.1   Reverberation Mapping

Reverberation mapping is based on the premise that the BLR reprocesses the ionising continuum from the central source into line emission, with a time delay proportional to the distance between the BLR and the central source. Thus, fluctuations in the ionising continuum propagate out to changes in the line emission at later times. Under the assumption that the time taken for the wind ionisation state to equilibrate to changes in the ionising continuum, then the total luminosity of a line L at a given time t is proportional to changes in the continuum ΔC at a range of previous times $t - \tau$ and the *response function* $\Psi_R(t)$ as equation 1:

$$\Delta L(t) = \int_0^\infty \Delta C(t - \tau)\Psi_R(\tau)d\tau. \tag{1}$$

The response function describes how a pulse in continuum luminosity ΔC is spread across a range of time τ. For a simple emission geometry, e.g. emission from a thin shell at a single radius from the central source, this factor is determined by the relative difference in path from light travelling from various parts of the shell to the observer. For a more complex emission geometry, $\Psi_R(t)$ *also* folds in the fact that emission occurs at a range of radii, and may not be symmetric. As a result a 1-dimensional response function, whilst comparatively easy to recover from observations, is

highly degenerate. More information can be recovered from a 2-dimensional velocity-resolved response function generated from spectra with sufficient spectral resolution to determine the Doppler shift v across a line, as equation 2:

$$\Delta L(v, t) = \int_0^\infty \Delta C(t - \tau)\Psi_R(v, \tau)d\tau. \tag{2}$$

For a 2-dimensional velocity-resolved response function, much of the degeneracy in Ψ_R is broken as only some portions of the observer-projected velocity/delay space are available to any given geometry, and characteristic $\Psi_R(v, t)$ can be produced for a range of geometries (Horne et al. 1991). Figure 1 illustrates how inflows and outflows in particular have very different profiles in $\Psi_R(v, t)$. As outflows reach the highest negative velocity relative to the observer (i.e. in the opposite direction to the observer) on the opposite side of the system to the observer, line photons with that Doppler shift are delayed by $2R_{max}/C$ relative to those shifted by motion *towards* the observer, with the opposite being true for inflow. Rotation tends to produce a $Psi_R(v, t)$ signature with a symmetric Doppler shift. In a physically-motivated model, such as the 'Occam's Quasar' disk wind of Matthews et al. (2016) 2, we would expect to see a mix of signatures corresponding to the different kinematic components of the wind. In addition, when ionisation is taken into account, we would expect changes in the driving ionising continuum to change the geometry of the emission regions for a given line (Mangham et al. 2017). This could potentially lead to negative responses for some parts of the velocity-delay space, as the associated sections of the wind become overionised and stop emitting.

2.2   Inversion

The velocity-resolved transfer function $\Psi_R(v, t)$ of a system can be recovered from a time series of spectral observations of sufficiently high wavelength resolution and a light-curve of the driving continuum responsible. Different techniques exist to accomplish this; the two tested in this paper (Pancoast et al. (2011) and Horne et al. (1991)) are discussed in sections 3.4.1 and 3.4.2 respectively.

> Leave the discussion of inversion to the experts?

3   METHODS

3.1   Fundamentals

The radiative transfer and ionisation code Python used has already been described several times in the literature (Long & Knigge 2002; Sim et al. 2005; Noebauer et al. 2010; Higginbottom et al. 2013; Higginbottom et al. 2014; Matthews et al. 2015, 2016), so we give only a brief description of it here. Python was originally designed to produce synthetic spectra for compact object modelling using iterative radiative transfer and ionisation. A central source, disk and a disk wind (following the Shlosman & Vitello (1993) prescription) are specified. The code performs a Monte Carlo radiative transfer simulation, simulating the paths of photons generated by the central source, disk and wind through the system. It records their interactions with the wind on a grid, including their contributions to local heating and ionisation. After sufficient photons have been run to attain low Poisson
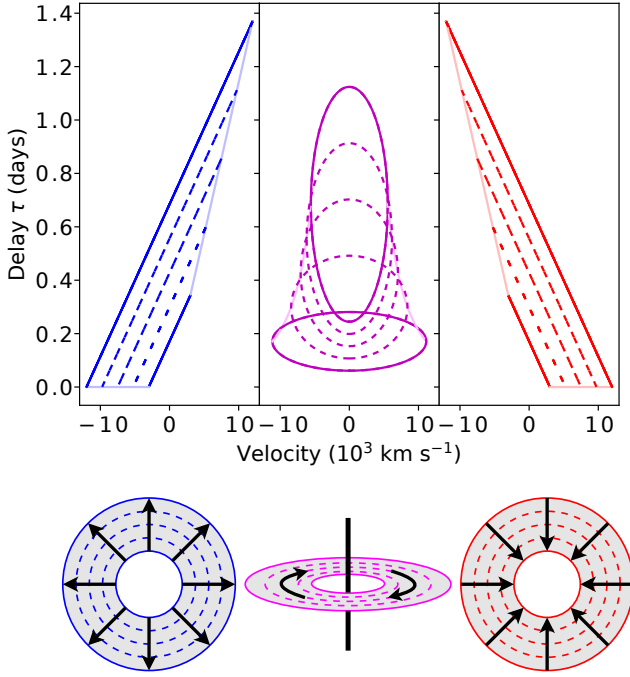
Figure 1. Outline response functions and schematics for Hubble-type spherical outflow **(left)**, a rotating Keplerian disc viewed at a 20° angle **(centre)**, and Hubble-type spherical inflow **(right)**. Winds extend from $r_{min} = 20r_g$ to $r_{max} = 200r_g$ for an AGN of mass $10^7 M_\odot$. Hubble out/inflows have $V(r_{min}) = \pm 3 \times 10^3$ km s^{-1}. Solid lines denote the response from the inner and outer edges of the winds, dotted lines from evenly-spaced shells within the wind. Pale lines describe the edge of the velocity-delay shape of the response function.

noise in the important regions of the wind, the temperature and ionisation state of each wind cell is updated. This changes the emission profile and opacity of the wind, requiring that the radiation transfer process be repeated. The ionisation state is then recalculated, and this process is iterated until the temperature and ionisation state of the wind has converged. Once a converged wind has been produced, this is then used to generate detailed spectra for photons for a range of user-specified observation angles.

We use the code to generate response functions using the methodology as described in Mangham et al. (2017), which we briefly describe here. The response function, Ψ_R, is a measure of how the change in emission of a given line at time t depends upon changes in the continuum at a range of previous times $t - \tau$. This requires making the assumption that the response function is *not* dependent on the continuum luminosity. If this is the case, then the response function can also be mirrored in time; it describes not only how emission at time t depends on the continuum at time $t - \tau$, but *also* how emission at time t propagates out to change emission at time $t + \tau$. As a result of this, we can derive the response function Ψ_R by forward-modelling. The change in emission at a range of times $t + \tau$ as the result of an instantaneous change in continuum luminosity at time t can be calculated by tracking the photons in our Monte Carlo simulation and calculating their arrival time delay τ from their
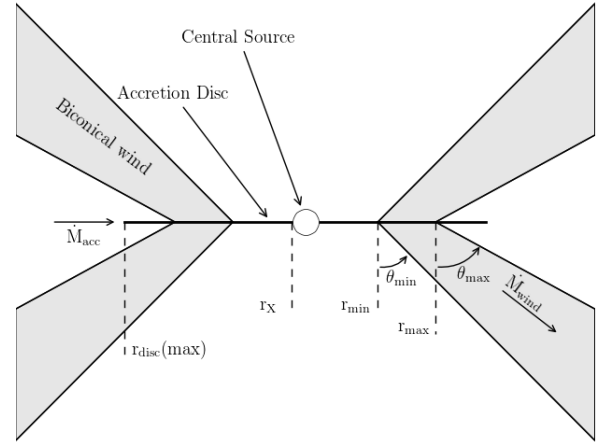

Figure 2. Sketch of the biconical disc wind geometry from Matthews et al. (2016).

path. These photons are then binned by velocity and delay to produce a response function $\Psi_R(v, \tau)$.

Response functions are produced for the $H\alpha$ line in two systems; the Seyfert and QSO models from Mangham et al. (2017). These were chosen because they represent plausible, physically-motivated response function signatures and display a range of behaviours that allow us to investigate the capabilities of inversion tools to cope with both straightforward and unusual response functions. These are discussed further in section 3.2. Whilst $H\beta$ is more traditionally used in velocity-resolved reverberation mapping campaigns (Denney et al. 2009; Doroshenko et al. 2012), our models do not currently produce enough $H\beta$ emission to produce a detailed velocity-resolved response function on a reasonable time-scale (simulation times on the order of $\approx$ weeks).

3.2 Generating Time Series of Spectra

Equation 2 describes how the changes in ionising continuum relate to changes in the luminosity of an emission line via the response function. What we *actually* have access to from observation is not the raw ΔL, but a time series of spectra. In the limit of small changes in ionising continuum luminosity, we can assume that the response function Ψ_R is constant. In this case, we can assume that the spectra $L(v, t)$ can be expressed straightforwardly as deviation from a base spectrum $L_0(v)$ as equation 3.

$$L(v, t) = L_0(v) + \int_0^\infty \Psi_R(v, \tau) \Delta C(t - \tau) d\tau \qquad (3)$$

As part of this method, we generate a time series of spectra for a mock observing campaign. We create a time series of 101 spectra over 100 days, timed to be simultaneous with our continuum luminosity measurements. This time-scale and count is comparable to existing observation campaigns (Du et al. 2014; De Rosa 2015).

We initialise each spectrum in the time series to a base spectrum taken from an assumed mean luminosity model. Then, we create a grid in time between the initial and

last continuum measurement, with spacing equivalent to the smallest bin in our discretised response function $\Psi_{RB}(v,t)$. For each step in this grid t_S, we perform simple linear interpolation to arrive at the value of the driving continuum C and thus the deviation from the mean luminosity $\Delta C(t_S)$. Then, starting at the initial time-step, we apply the contribution from the change in luminosity ΔC to the spectrum at each later time-step $t_S + \tau$ as $\Psi_{RB}(v,\tau)\Delta C(t_S)$. Continuing this process for every time-step, the result is equivalent to equation 4. A diagram of this process for a toy transfer function can be shown in figure 4. The more physically-motivated design behind this implementation (seeking to mimic the actual process giving rise to the response function) makes it relatively intuitive, and offers the scope for further development. In particular, it would be possible to allow for *continuum-dependent response functions*, though that is not within the scope of this work.

$$L(v,t) = L_0(v) + \sum_{t_S} \Psi_{RB}(v, t - t_S)\Delta C(t_S) \qquad (4)$$

When generating time-series for Caramel, which requires a continuum-subtracted spectrum, we set L_0 to the continuum-subtracted base spectrum from the mean luminosity model, using a linear fit to subtract the continuum under the line. MEMEcho instead requires regions of continuum either side of the line, and the method is slightly modified to apply changes in the continuum luminosity to the spectrum as equation 5.

$$L(v,t) = L_0(v) + \Delta C(v,t) + \sum_{t_S} \Psi_{RB}(v, t - t_S)\Delta C(t_S) \qquad (5)$$

As a proxy for our driving ionising continuum, we use the 1158 light-curve of NGC5548 from Fausnaugh et al. (2016). This provides us with a realistic base to begin with. The light-curve is rescaled to match the mean luminosity for each model, and the range of variation is reduced to ±50% about this mean value. Our original goal was to rescale to ±10%, though this resulted in datasets with insufficient variation to be successfully modelled by Caramel (see figure 3). We also rescale in time the response maps used to produce the time series. In order to match the average ≈ 30 day delays seen in Hβ for NGC5548 (Bentz et al. 2013), we rescale them in time to a peak delay of ≈ 30 days. We then generate the errors on the spectra for each time series. Caramel is used to input time series for emission where the ratio of the mean integrated line flux error ϵ_L to the line variation ΔL is on the order of $0.01 - 0.03$. For the QSO Ψ_R, we set a constant error in each spectral bin ϵ_{LB} to satisfy equation 6, aiming to replicate a relatively accurate dataset. Setting lower errors led to over-fitting issues with Caramel, impairing its ability to fit our time series data on a practical time-scale ($\approx$ weeks to months, see section 3.4.1).

$$\frac{\epsilon_L}{\Delta L} = \frac{\sqrt{n_{\text{bins}}}\epsilon_{LB}}{\Delta L} = 0.02 \qquad (6)$$

The anti-correlation of the line light-curve with the continuum for the Seyfert Ψ_R made the line variation method inapplicable. Instead, we applied a fixed error $\epsilon_{LB,\text{Sey}}$ to each bin of the Seyfert spectrum to attain the same signal to noise ratio for the line peak as the QSO spectrum. These
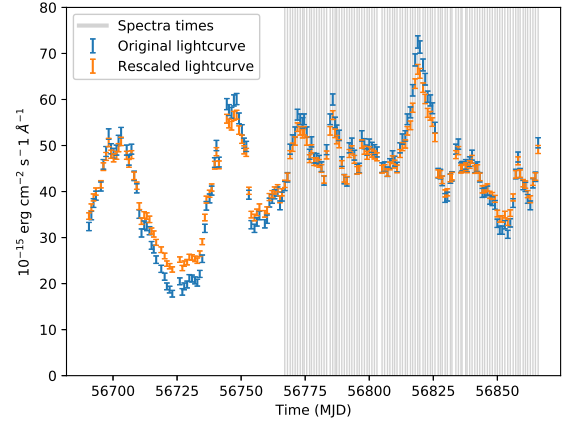

Figure 3. Original and rescaled driving light-curves used in generating time series of spectra, taken from NGC5548 (Fausnaugh et al. 2016).

errors were then used to apply a Gaussian error to each bin of our dataset, to get a 'noisy' spectrum. These final time-series of spectra are shown in figures 5 and 6.

3.3 Blinding

We aimed to conduct a blinded trial of both the Caramel and MEMEcho deconvolution techniques. In order to replicate the process for recovery from observational data as closely as possible, neither group was provided with a copy of the response function used to generate the time-series. Instead, both were provided with the time-series for the QSO and Seyfert models in their preferred input format, as well as the rescaled continuum light curves used to generate them.

3.4 Inversion Methods

3.4.1 CARAMEL

Pending

3.4.2 MEMEcho

Pending

4 RESULTS

4.1 QSO Ψ_R

The *'true'* response function of our QSO system is shown in figure 7. The striping effects visible in the response are artefacts of our simulation grid. Removing them entirely would require an impractically high resolution.
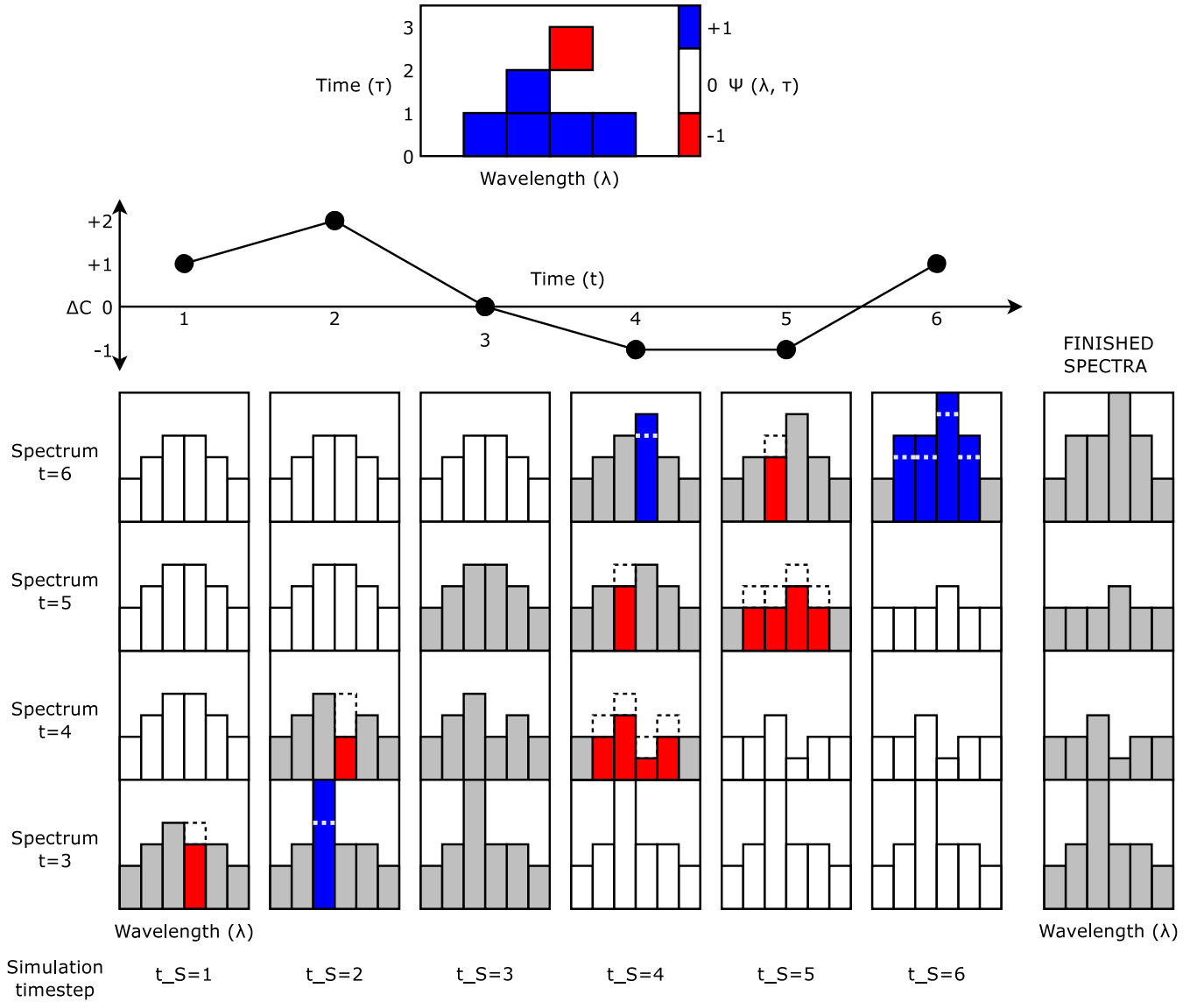
Figure 4. Diagram showing how a discretised toy transfer function $\Psi(\lambda, t)$ (top) applies changes in continuum luminosity ΔC to a base spectrum to form a series of spectra at times $t = 3-6$. Each column of spectra in the lower section shows the final spectra being constructed over each simulation time-step t_S. Within a spectrum, columns in **red** indicate a wavelength bin whose flux has been *decreased* this simulation time-step, columns in **blue** a wavelength bin whose flux has been *increased*, and columns in grey a wavelength bin whose flux is unchanged. Columns in **white** are those outside of the $t_S + \tau$ range the response function applies to, and so were *ineligible* to be changed this time-step. Final spectra are the rightmost column, in grey.

4.1.1 CARAMEL

Show figure (fig 8)

Pending

4.1.2 MEMEcho

Show figure (fig 9).

Pending

4.2 Negative Ψ_R

Show figure (fig 10).

Pending

Pending

5 DISCUSSION

5.1 Positive Ψ_R

- Differences between methods
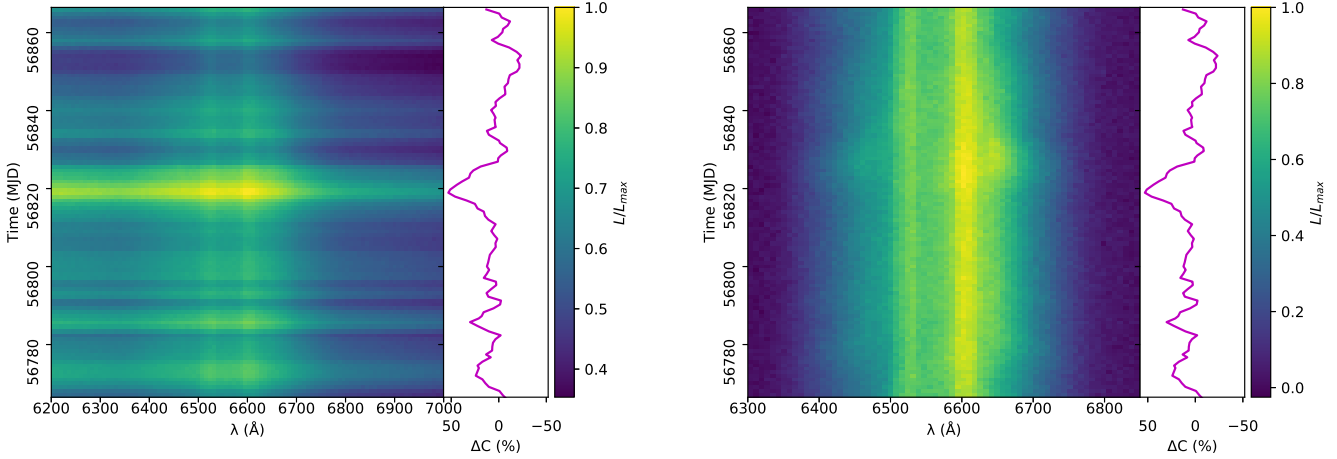- Differences to true result
- Similarities
- Limits on conclusions

Figure 5. Trailed spectrogram generated for the full (left) and continuum-subtracted (right) Hα line of our QSO model over a simulated observing campaign of 98.9 days.
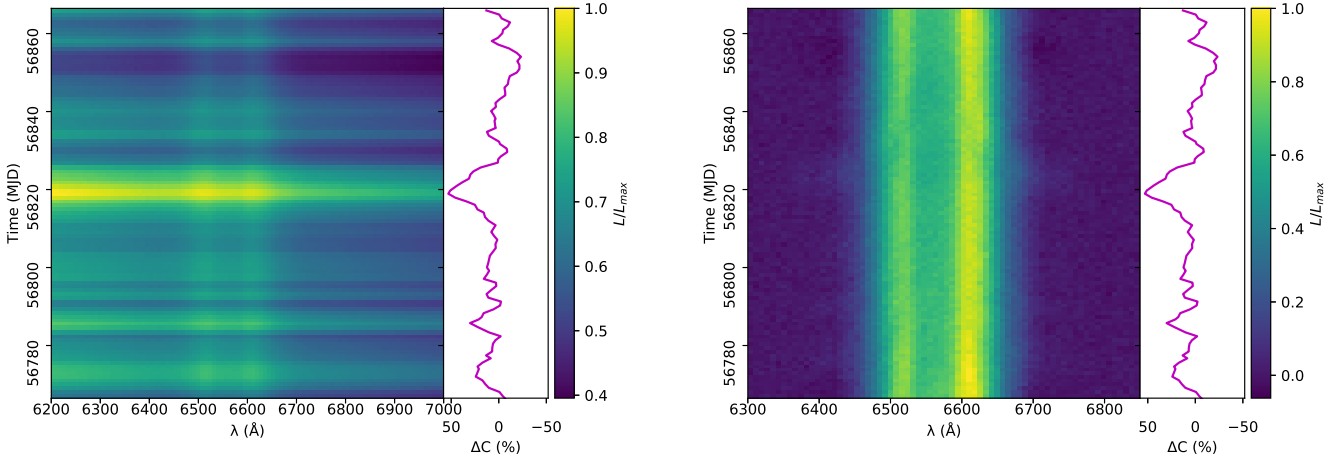

Figure 6. Trailed spectrogram generated for the full (left) and continuum-subtracted (right) Hα line of our Seyfert model over a simulated observing campaign of 98.9 days.

5.2 Negative Ψ_R

- Differences between methods
- Differences to true result
- Similarities
- Limits on conclusions

6 CONCLUSIONS

ACKNOWLEDGEMENTS

REFERENCES

Bentz M. C., et al., 2008, ApJ, 689, L21
Bentz M. C., et al., 2010, ApJ, 720, L46
Bentz M. C., et al., 2013, ApJ, 767, 149
De Rosa G., 2015, IAU General Assembly, 22, 2257825
De Rosa G., et al., 2015, ApJ, 806, 128
Denney K. D., et al., 2009, ApJ, 704, L80
Doroshenko V. T., Sergeev S. G., Klimanov S. A., Pronik V. I., Efimov Y. S., 2012, MNRAS, 426, 416
Du P., et al., 2014, ApJ, 782, 45
Du P., et al., 2016, ApJ, 820, 27
Fausnaugh M. M., et al., 2016, ApJ, 821, 56
Gaskell C. M., 1988, ApJ, 325, 114
Grier C. J., 2013, PhD thesis, The Ohio State University
Grier C. J., et al., 2013, The Astrophysical Journal, 764, 47
Higginbottom N., Knigge C., Long K. S., Sim S. A., Matthews J. H., 2013, MNRAS, 436, 1390
Higginbottom N., Proga D., Knigge C., Long K. S., Matthews J. H., Sim S. A., 2014, ApJ, 789, 19
Horne K., 1994, in Gondhalekar P. M., Horne K., Peterson B. M., eds, Astronomical Society of the Pacific Conference Series Vol. 69, Reverberation Mapping of the Broad-Line Region in Active Galactic Nuclei. p. 23
Horne K., Welsh W. F., Peterson B. M., 1991, ApJ, 367, L5
Kaspi S., Netzer H., 1999, ApJ, 524, 71
Kaspi S., Maoz D., Netzer H., Peterson B. M., Vestergaard M., Jannuzi B. T., 2005, ApJ, 629, 61
Koratkar A. P., Gaskell C. M., 1989, ApJ, 345, 637
Long K. S., Knigge C., 2002, ApJ, 579, 725
Mangham S. W., Knigge C., Matthews J. H., Long K. S., Sim S. A., Higginbottom N., 2017, Monthly Notices of the Royal Astronomical Society, 471, 4788
Matthews J. H., Knigge C., Long K. S., Sim S. A., Higginbottom N., 2015, MNRAS, 450, 3331

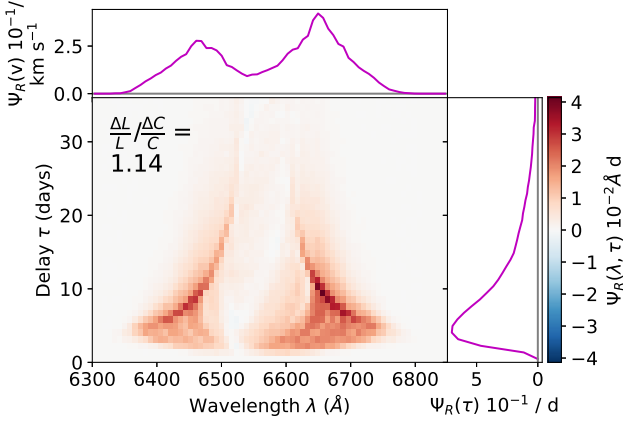**Figure 7.** The 'true' velocity-resolved response function (lower) for Hα in the QSO model, rescaled to a peak delay of ≈ 3 days.
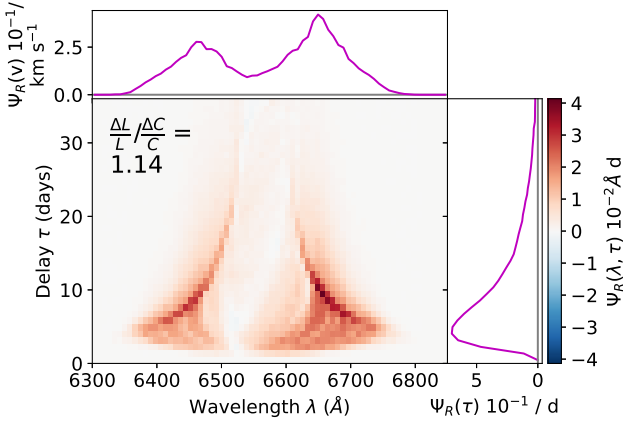

Figure 8. The response function for Hα in the QSO model, as reconstructed by CARAMEL. NOTE DIFFERENCES, PARTIC-ULARLY IN TIME AND RESPONSE
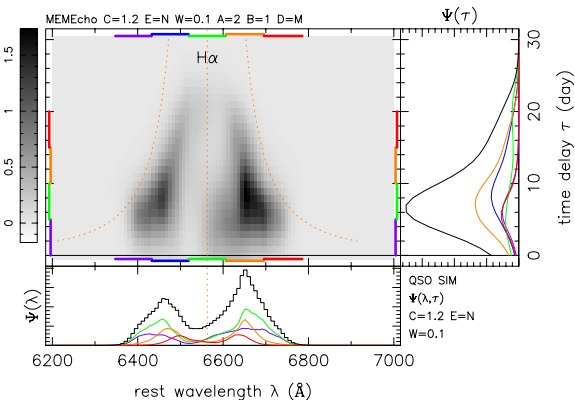

Figure 9. The response function for Hα in the QSO model, as reconstructed by MEMEcho. NOTE DIFFERENCES, PARTIC-ULARLY IN TIME AND RESPONSE
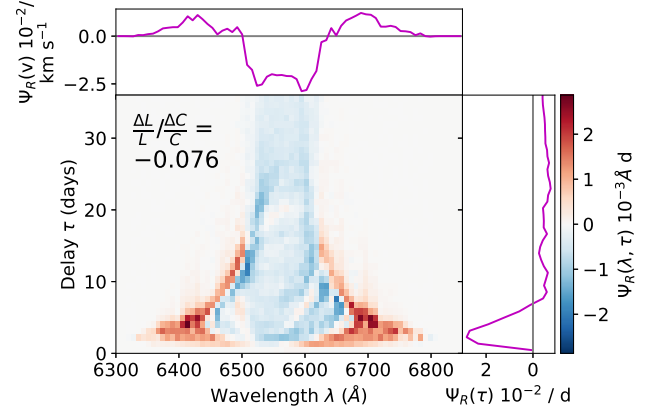

Figure 10. The 'true' velocity-resolved response function (lower) for Hα in the Seyfert model, rescaled to a peak delay of ≈ 3 days.

Matthews J. H., Knigge C., Long K. S., Sim S. A., Higginbottom N., Mangham S. W., 2016, MNRAS, 458, 293
Noebauer U. M., Long K. S., Sim S. A., Knigge C., 2010, AJ, 719, 1932
Onken C. A., Ferrarese L., Merritt D., Peterson B. M., Pogge R. W., Vestergaard M., Wandel A., 2004, ApJ, 615, 645
Pancoast A., Brewer B. J., Treu T., 2011, ApJ, 730, 139
Pancoast A., Brewer B. J., Treu T., 2014, MNRAS, 445, 3055
Peterson B. M., 1993, PASP, 105, 247
Shlosman I., Vitello P., 1993, ApJ, 409, 372
Sim S., Drew J., Long K., 2005, MNRAS, 363, 615
Ulrich M.-H., Horne K., 1996, MNRAS, 283, 748
Welsh W. F., Horne K., 1991, ApJ, 379, 586

This paper has been typeset from a TeX/LaTeX file prepared by the author.